Response of the Geospace System to the Solar Wind Dynamic Pressure Decrease on 11 June 2017: Numerical Models and Observations

Dogacan S. Ozturk[1], Shasha Zou[2], James A. Slavin[2], Aaron J. Ridley[2]

[1]Jet Propulsion Laboratory, California Institute of Technology, Pasadena, California, USA
[2]Department of Climate and Space Sciences and Engineering, University of Michigan, Ann Arbor, USA

Key Points:

- The decrease in the solar wind dynamic pressure led to two separate pairs of oppositely rotating vortices in the dawn and dusk.
- FACs accompanied each magnetospheric vortex and altered the ionosphere convection patterns.
- Joule heating increased in the regions sandwiched by the perturbation FACs, leading to increased ion temperatures.

Author Manuscript

This is the author manuscript accepted for publication and has undergone full peer review but has not been through the copyediting, typesetting, pagination and proofreading process, which may lead to differences between this version and the Version of Record. Please cite this article as doi: 10.1029/2018JA026315

Corresponding author: Dogacan S. Ozturk, Previously in (2), dogacan.s.ozturk@jpl.nasa.gov

This article is protected by copyright. All rights reserved.

Author Manuscript

Abstract

On 11 June 2017, a sudden solar wind dynamic pressure decrease occurred at 1437 UT according to the OMNI solar wind data. The solar wind velocity did not change significantly, while the density dropped from 42 cm^{-3} to 10 cm^{-3} in a minute. The IMF B_Z was in weakly northward during the event, while the B_Y changed from positive to negative. Using the University of Michigan Block Adaptive Tree Solarwind Roe Upwind Scheme (BATS-R-US) global magnetohydrodynamics (MHD) code, the global responses to the decrease in the solar wind dynamic pressure were studied. The simulation revealed that the magnetospheric expansion consisted of two phases similar to the responses during magnetospheric compression, namely a negative preliminary impulse and a negative main impulse phase. The simulated plasma flow and magnetic fields reasonably reproduced the THEMIS and MMS spacecraft in situ observations. Two separate pairs of dawn-dusk vortices formed during the expansion of the magnetosphere, leading to two separate pairs of Field-Aligned Current (FAC) cells. The effects of the flow and auroral precipitation on the I-T system were investigated using the Global Ionosphere Thermosphere Model (GITM) driven by simulated ionospheric electrodynamics. The perturbations in the convection electric fields caused enhancements in the ion and electron temperatures. This study shows that, like the well-studied sudden solar wind pressure increases, sudden pressure decreases can have large impacts in the coupled I-T system. In addition, the responses of the I-T system depend on the initial convection flows and FAC profiles before the solar wind pressure perturbations.

1 Introduction

Sudden variations in the solar wind dynamic pressure cause global changes in the magnetospheric configuration, disrupt the magnetospheric and ionospheric current systems and result in large scale flow perturbations (Samsonov and Sibeck (2013), Kivelson and Southwood (1991), Fujita et al. (2003a), Fujita, Tanaka, Kikuchi, Fujimoto, and Itonaga (2003b), Yu. and Ridley (2011)). The response of the geospace system to the sudden enhancements of the solar wind dynamic pressure, known as sudden storm commencements (SSCs) or sudden impulses (SIs), (Araki (1994a)) has been traditionally studied using ground magnetometer observations. These ground magnetometer observations show temporal, latitudinal, and longitudinal dependencies (Araki (1994a), Araki (1994b), Sun et al. (2014)) indicating that they may be due to the different magnetospheric and ionospheric sources (Fujita et al. (2003a), Fujita et al. (2003b), Kivelson and Southwood (1991)). The high-latitude magnetometer observations of SIs show that the compression signature can be decomposed as a short-lived Preliminary Impulse (PI) and a succeeding longer-lived Main Impulse (MI) (Araki (1994a), Araki (1994b)). The combination of these impulse signatures create a bipolar response, with its polarity dependent on the magnetic local time (MLT) and magnetic latitude. Investigating the physical processes being dependent on the formation and propagation of the SI signatures is an important aspect of understanding solar wind-magnetosphere interaction.

Apart from the SI events related to the solar wind dynamic pressure enhancements, which will be referred to as SI^+ from here on, the solar wind dynamic pressure decreases can also cause global disruptions in the geospace system. Araki and Nagano (1988) showed that high-latitude ground magnetometers observed bipolar responses with opposite polarities to those of SI^+s, during sudden expansions of the magnetosphere after the solar wind dynamic pressure dropped. In addition, they used geosynchronous spacecraft measurements to show that the magnetic field parallel to Earth's rotation axis decreased as a result of expansion. Ground magnetometer observations at lower latitudes showed that this decrease was preceded by a short-lived initial positive perturbation. Except this initial positive perturbation at the low-latitudes, they concluded that SI^-s can be explained by the "mirror image" of the same model derived for SI^+s (Araki, 1994a). Only five events were investigated in this early study, and more events are needed to conclusively determine whether the SI^- events are mirror images of the SI^+ events.

This article is protected by copyright. All rights reserved.

Author Manuscript

To explain the distribution and the polarization of the SI^-s further, Takeuchi et al. (2000), conducted a study using higher temporal resolution ground magnetometer data and further distinguished the SI^- signatures from that of an opposite SI^+ at certain locations on the ground. They investigated the SI^- response with a larger data set consisting of 28 events (Takeuchi, Araki, Viljanen, & Watermann, 2002), and confirmed that the SI^- generation can be explained by simply reversing the direction of the electric field in the equatorial plane that occurs due to the sunward motion of the magnetopause. They suggested that magnetospheric compression and expansion mechanisms lead to oppositely rotating ionospheric vortices. They concluded that similarities arise between SI^+ and SI^- signals based on the relative location of the ground magnetometers to the overhead vortices.

As opposed to the SI^+s, there is no strong link between geomagnetic storms and SI^-s since they are usually associated with reverse shocks, but studies have been carried out investigating the relationship between SI^-s and geomagnetic activity. Sato et al. (2001) was the first one to show that the optical aurora can be enhanced due to solar wind dynamic pressure drops. They investigated a sharp dynamic pressure decrease from 12 nPa to 2 nPa and used DMSP satellite measurements to show enhanced electron precipitation, and an associated upward FAC system at dusk. They argued that field line resonance might be the reason for the acceleration of electrons, as opposed to loss-cone instability which is responsible for the enhanced optical emissions during SI^+s (Zhou and Tsuratani (1999)). Liou (2007) further investigated the link between SI^-s and geomagnetic activity with a data set of 13 large solar wind dynamic pressure drop events. Using the ultraviolet imager on the Polar satellite and ground magnetometer observations, they found that 3 of the 13 events were associated with substorms, and an increase in the open flux was necessary to trigger a substorm regardless of the magnitude of the dynamic pressure drop. Another optical emission study by Belakhovsky and Vorobjev (2016) showed that a nightside substorm occurred as a response to the SI^-. During the studied event, the pressure drop was accompanied by a further southward turning of the IMF. This is consistent with the Liou (2007) results that more magnetic flux is needed for a substorm to occur.

There are many studies that investigate the magnetospheric and ionospheric sources of the two-step response (PI^+ and MI^+) during a solar wind dynamic pressure enhancement event. Most of these studies identify magnetospheric vortices as the source of MI^+ perturbation (Sibeck (1990), Keller et al. (2002), Fujita et al. (2003b), Samsonov, Sibeck, and Yu (2010), Yu. and Ridley (2011), Samsonov and Sibeck (2013), Sun et al. (2014), Tian et al. (2016), Ozturk, Zou, and Slavin (2017), Ozturk, Zou, Ridley, and Slavin (2018)), however the source of PI^+ perturbation is attributed to different mechanisms. Some of the proposed mechanisms are shock intensified lobe reconnection (Samsonov et al. (2010)), dusk to dawn electric fields at the magnetopause (Yu. & Ridley, 2011), transverse waves excited by the fast magnetosonic waves (Tamao (1965),Araki (1994a)), localized solar wind impulses (Kataoka, Fukunishi, Fujita, Tanaka, & Itonaga, 2004) and magnetospheric vortices (Kivelson & Southwood, 1991). However, another study conducted by Samsonov, Nemecek, and Safrankova (2006) showed that an interplanetary shock propagation can generate various different responses like slow expansion waves, contact discontinuities and slow reversed shocks, depending on the magnetospheric conditions at the time of the shock passage. They concluded that the identification of these perturbations through measurements would be difficult due to the similarity in their propagation velocities.

The generation mechanisms of the two-step response to SI^- events are thought to be the mirror-image of the SI^+ events (Takeuchi et al. (2002), Fujita, Tanaka, Kikuchi, and Tsunomura (2004), Zhang et al. (2010)), but most of the aforementioned magnetospheric expansion studies relied on scarce observational data. One important modeling work on SI^-s was conducted by Fujita et al. (2004). Their simulation results confirmed that similar to the SI^+, oppositely directed FAC pairs form as a result of magnetospheric expansion, namely during the PI^- and MI^- phases. Revisiting this study, Fujita, Yamagishi, Murata, Den, and Tanaka (2012) found out that both PI^- and MI^- FACs were associated

This article is protected by copyright. All rights reserved.

Author Manuscript

with oppositely rotating magnetospheric vortices, followed by a third magnetospheric vortex system that was not previously reported during the SI^+s, indicating that the generation mechanisms of magnetospheric perturbations can differ. Fujita et al. (2012) was the first to link both FAC perturbations to magnetospheric vortices. More recently, Zhao et al. (2016) used equivalent ionospheric currents deduced from ground magnetometer observations and THEMIS observations together with an MHD simulation, and identified the magnetospheric source region of observed ionospheric vortices. Their results showed a counter clockwise rotating vortex in the dawn sector in the equatorial magnetosphere during the MI^- phase as a result of the magnetospheric expansion.

In this paper, a sudden solar wind dynamic pressure decrease is investigated using global MHD and I-T models as well as in situ spacecraft and ground magnetometer observations. The purpose of this study is to investigate the magnetospheric and ionospheric sources for the PI^- and MI^- signatures, determine the polarity distribution of the ground magnetometer responses to SI^-s, identify the ionospheric regions which are most prone to SI^- events and understand how the ionosphere and thermosphere systems are affected in those regions.

2 Methodology

2.1 Simulation Setup

The 11 June 2017 1430-1500 UT interval was chosen to study the effects of the sudden solar wind dynamic pressure decreases on the geospace system. The Global Magnetosphere (GM), Inner Magnetosphere (IM) and Ionospheric Electrodynamics (IE) modules of the Space Weather Modeling Framework (SWMF) (Toth et al., 2005) were coupled to represent the magnetosphere system. The GM module, i.e. BATS-R-US, is used to solve for ideal MHD equations in GM domain and is two-way coupled with the Rice Convection Model (RCM) (Toffoletto, Sazykin, Spiro, & Wolf, 2003) that models the inner magnetosphere kinetic physics. Taking the time dependent magnetic and electric field input from the GM module, RCM calculates the ExB and gradient curvature drifts to solve the particle transport equations. The GM module then transfers the field-aligned currents including the IM region, to the high-latitude electrodynamics model. The Ridley Ionosphere Model (RIM) was used (Ridley, Gombosi, & DeZeeuw, 2004) as the IE model. When coupled with global and inner magnetosphere models, it takes the Region-1 and Region-2 currents at the top of the ionosphere and generates a conductance pattern based on an empirical relation and calculates the electric field potentials, which are then passed back to the GM module.

For this case study, the GM inner boundary is set to 2.5 R_E from the center of the Earth. The computational domain is a three-dimensional box in geocentric solar magnetospheric (GSM) coordinates that starts from 32 R_E upstream of the Earth in the X direction to 224 R_E tailward and -128 R_E to +128 R_E both in the Y and Z directions. The finest resolution is 1/8 R_E grid close to the Earth. 600 virtual ground magnetometers are implemented in both hemispheres uniformly from the magnetic equator up to 80° latitude (4° in latitude by 12° in longitude). The solar wind and IMF data from the OMNI Database, are used to drive the model, which were propagated to the bow shock nose and are shown in Figure 1a.

Since the drivers for the simulation are taken from the OMNI Database, the simulation times are shifted back by 7 minutes, which is roughly the time for the solar wind to propagate from 32 R_E, the outer boundary of the simulation domain, to the Earth bow shock nose with the solar wind speed. Figure 1b shows the IMF and solar wind parameters extracted at the subsolar point, x=17 R_E from the simulation. The green line shows the arrival of the solar wind dynamic pressure drop that impacted the Earth a couple of minutes later. The IMF B_Y was positive before the event, around 5 nT, but turned negative at 1438 UT and stayed around -10 nT during the event. The IMF B_Z was northward and did not show any strong variations during the interval. The change in solar wind velocity was small, around 20 km/s, during the event with no significant variations, but the solar wind density

This article is protected by copyright. All rights reserved.

Author Manuscript

Figure 1. The IMF B_Y, B_Z, solar wind V_X, N_P, P_{dyn} and $sym-H$ values from OMNI solar wind database for the time interval between 1400-1500 UT (a) and the same parameters (except sym-H) extracted from the simulations at the subsolar point [17 R_E] for the time interval between 1420-1450 UT (b) are shown. The solid green line shows the time of the pressure drop.

This article is protected by copyright. All rights reserved.

Author Manuscript

dropped from 42 cm^{-3} to 10 cm^{-3}. Therefore, the solar wind dynamic pressure dropped from around 8 nPa to 2 nPa. As the magnetosphere expanded, the outward motion of the magnetopause led to a reduction of the dawn-to-dusk magnetopause current. Consequently, the sym-H index dropped from 25 nT to 0 nT due to this dynamic pressure decrease.

The GITM simulations were driven with the OMNI solar wind data before the event, from 9 June 2017 1400 UT to 11 June 2017 1400 UT. The Weimer (2005) empirical model was used for the convection potential, while the Ovation aurora model [Newell et al. (2002)] was used for particle precipitation during this interval. The particle precipitation and electric field solutions obtained from the global MHD model were then used to drive the GITM simulations starting from 11 June 2017 1400 UT to 1500 UT, updating the electrodynamic patterns every 10 seconds. The GITM simulations were run with a spatial resolution of 4° in longitude and 1° in latitude and an altitude range between 100 and 600 km.

2.2 Spacecraft Positions

Both THEMIS-D and MMS measured perturbations associated with the pressure change. The locations of the THEMIS-D and MMS-1 spacecraft are shown in Figure 2. THEMIS-D was located in the dayside afternoon sector [3.4, 10.7, -2.1 R_E], very close to the magnetopause before the decompression, while MMS-1 was located in the tail dawn sector [-22.4, -9.9, 5 R_E] during the event. The ESA instrument from THEMIS-D was used to understand the magnetospheric flows at this location whereas the FGM instrument from MMS-1 was used to understand the change in magnetic field configuration.

3 Results

3.1 Magnetospheric Response

Figures 3 and 4 show the evolution of the global magnetosphere system before and during the decompression. The temporal variation of the pressure profile in the XZ plane is shown in Figures 3 a-b, including the locations of the MMS-1 and THEMIS-D spacecraft. The white dots show the location of the magnetopause lobe boundary and the pink dots close to the Z = 0 plane mark the current sheet boundary. The front of the dynamic pressure drop can be seen as the red to blue transition propagating near 13 R_E at 1435 UT and 5 R_E at 1438 UT. The equatorial flow profile can be seen on the right (Figures 3 c-d) with the solar wind and magnetosheath flow vectors.The contour colors represent the x component of the flow velocity. There were two channels of sunward flows located around X=2 R_E, Y=7 R_E and X=6 R_E,Y=-6R_E just before the decompression.

At 1438 UT, shown in Figures 3b and d, the nose of the magnetopause started to expand sunward. This resulted in two partial flow vortices at the dayside magnetosphere, one having a counter clockwise sense of rotation in the dusk sector (marked with number 1) and the other having a clockwise sense of rotation in the dawn sector (marked with number 2). These vortices will be referred to as PI^- vortices from here on. There were also significant sunward flows at the nose of the subsolar magnetopause. The top panels of Figure 4 (a-d) show the magnetospheric response at 1440 UT when the low density region in the solar wind propagated to X=-2 R_E. The expansion of the magnetosphere in the downstream, shown in the XZ plane in Figures 4 b-c, caused significant perturbations in the magnetotail. Near the location of the MMS-1 spacecraft, the magnetotail was no longer as highly stretched as it was during the compressed state, leading to a decrease in the B_X and an increase in the B_Z components, becoming more dipolarized. In the equatorial plane, shown in Figures 4 e-f, a new pair of flow vortices emerged with opposite senses of rotation to the PI^- vortex at dusk (marked as 3) and dawn (marked as 4). Both pairs of vortices emerged inside the dayside magnetopause and propagated towards the nightside, eventually dissipating around 1450 UT (Figures 4 c-f). These vortices will be referred to as MI^- vortices from here on.

This article is protected by copyright. All rights reserved.

Author Manuscript

Figure 2. The positions of the MMS-1 (blue arrow) and THEMIS-D (red arrow) spacecraft are shown in GSM XY (a) and XZ (b) coordinates between 1430 UT to 1500 UT. The magenta dashed lines show the magnetopause boundary calculated with the Shue model, based on the IMF and solar wind values before the dynamic pressure drop. The teal dashed lines show the magnetopause boundary after the dynamic pressure drop.

This article is protected by copyright. All rights reserved.

Author Manuscript

This outward motion and flow perturbations occurred close to the THEMIS-D spacecraft location.

The evolution of the magnetopause location at the subsolar point was also investigated during this time interval as shown in Figure 5. The magnetopause location was calculated using the Shue model driven by the OMNI data, as well as the MHD simulated magnetopause location calculated using the density gradient method described in Garcia and Hughes (2007). At 1437 UT, the dynamic pressure dropped from 7.5 nPa to 2.4 nPa. The Shue model showed that the magnetopause location should have increased from $8.5R_E$ to $10R_E$, while the simulation results showed an expansion from $8R_E$ to $10R_E$, in agreement with the Shue model results.

Figure 6 shows the THEMIS-D ESA (a) and MMS-1 FGM (c) observations (blue) compared with the simulated satellite measurements (red). THEMIS-D initially recorded tailward flows in the dusk sector, however as the magnetosphere started to expand, the flows became sunward and then fluctuated around zero. The V_Y component was initially positive both in the simulations and the observations followed by fluctuations around zero. The simulated V_X and V_Y flow components agreed with the observations qualitatively. These results indicate that a series of flow perturbations were recorded in the dusk sector first with a sense of counter clockwise and then with a sense of clockwise rotation. Figure 6b shows the velocity hodograms of THEMIS-D measurements and SWMF results between 1430-1445 UT. Both simulations and observations show a counter clockwise rotation followed by a clockwise rotation, similar to the magnetospheric flow perturbations marked with 1 and 3 in Figures 3 and 4. The vortex calculated from the THEMIS-D hodogram shows that the PI^- vortex was around $2.6R_E$ in x and $2R_E$ in y, followed by the MI^- vortex which was around $6R_E$ in x and $6R_E$ in the y direction.

The MMS-1 FGM measurements presented in Figure 6c show the effects of the sudden pressure decrease front propagation to the tail. As a result of the decreased pressure, the magnetopause flaring angle increased, as indicated by a B_X decrease, and a B_Z increase as observed in the MMS-1 measurements, at 1445 UT. The time of arrival with the drop of B_X and enhancement of B_Z was captured by the simulation.

3.2 Ionospheric Response

Evolution of the FACs, perturbation FACs, the Joule heating (MHD definition $\Sigma_p E^2$, first term in Equation 5 of Thayer, Vickrey, Heelis, and Gary (1995)) and the horizontal magnetic perturbation profiles at the ground level were investigated to understand the ionospheric responses to the magnetospheric expansion. These maps are shown in Figure 7 at the same time cadences as the magnetospheric snapshots shown in Figures 3 and 4. Due to the IMF B_Z being northward, the FAC profile resembled the NBZ current system closely before the magnetospheric expansion. The Joule heating and magnetometer profiles at 1435 UT were chosen as the background conditions, and the values were subtracted from the following snapshots to highlight the effects of perturbation FACs. Figure 7b shows the responses 1 minute after the expansion started. The perturbation FAC systems, which were obtained by subtracting the FAC profile from the previous minute, clearly showed an upward FAC at dusk (1) and a downward FAC at dawn (2). The polarities of these FACs were consistent with the rotational sense of the magnetospheric flow vortices in Figure 3 marked with 1 and 2. The Joule heating maps shown in the third row of Figure 7b, increased slightly in between the perturbation FACs and decreased in the surrounding region. The magnetic field perturbations at the ground, shown in the fourth row of Figure 7b, indicated a positive perturbation (orange contours) at low latitudes between 3 to 19 MLT and in the high-latitude midnight sector. At the same time, the high latitude magnetic perturbation response near dawn was negative.

Figure 7c shows the perturbed profiles at 1440 UT. At this time, a new pair of perturbation FACs appeared with opposite polarities as the PI^- FACs. These MI^- FACs

This article is protected by copyright. All rights reserved.

Author Manuscript

Figure 3. The pressure contours in the XZ plane with open (black) and closed (white) magnetic field lines are shown on the left for 1435 UT (a), 1438 UT (b). The purple dot shows the location of THEMIS-D, whereas the pink dot shows the location of MMS-1. On the right, contours of V_X are plotted with magnetospheric flow vectors. The blue (red) contours on the top of Northern Hemisphere show the magnetic field lines centered at the flow vortices that carry downward (upward) FACs at 1438 UT. Numbers 1 and 2 show the magnetospheric flow perturbations at the negative preliminary impulse phase. Purple dots indicate the locations of the flow perturbations associated with vortices 1-2.

This article is protected by copyright. All rights reserved.

Author Manuscript

Figure 4. The pressure contours in the XZ plane with open (black) and closed (white) magnetic field lines are shown on the left for 1440 UT (a), 1445 UT (b) and 1450 UT (c). The purple dot shows the location of THEMIS-D, whereas the pink dot shows the location of MMS-1. On the right, contours of V_X are plotted with magnetospheric flow vectors. The blue (red) contours on the top of Northern Hemisphere show the magnetic field lines centered at the flow vortices that carry downward (upward) FACs at 1440 UT. Numbers 3 and 4 show the magnetospheric flow perturbations at the negative main impulse phase. Purple dots indicate the locations of the flow perturbations associated with vortices 1,2,3 and 4. The T shows the wave through and the R shows the wave ridge.

This article is protected by copyright. All rights reserved.

Author Manuscript

Figure 5. The variation of the magnetopause distance calculated with the Shue model (dashed) and density gradient (solid) with the solar wind dynamic pressure (green shading) in between 1430 UT to 1450 UT are shown.

This article is protected by copyright. All rights reserved.

Author Manuscript

Figure 6. The comparison of satellite measurements (blue) with simulated satellite responses (red) for (a) velocity measurements (Vx on top, Vy on bottom) from THEMIS-D ESA and (c) magnetic field measurements (Bx on top, Bz on bottom) from MMS-1 FGM are shown between 1430 UT-1450 UT. The middle panel (b) shows the velocity hodogram constructed using THEMIS-D ESA data (blue) and simulation results (red). The green shaded region for velocity measurements (a) marks the PI^{-} vortex, whereas the pink shaded region marks the MI^{-} vortex. The solid green line marks the arrival of the sudden dynamic pressure drop to the subsolar point at 1436 UT and the solid pink line shows the arrival of the decompression front to the MMS-1 location at around 1445 UT (c).

This article is protected by copyright. All rights reserved.

Author Manuscript

were upward in the dawn (4) and downward (3) in the dusk sectors. The PI^- FACs (1-2) had moved anti-sunward during this time. The Joule heating profile in the third row had increased clearly in the region between FACs 1-3 and 2-4, while weakened at the high-latitudes. The ground magnetic perturbations also showed a clear dawn-dusk asymmetry in this instance, with a positive perturbation around 70° and between 4-11 MLT but negative elsewhere. Combining Figure 7b and c, it can be seen that the positive perturbations at the lower-latitudes were short lived, similar to the observations shown in Araki and Nagano (1988).

At 1445 UT, the FAC profile started to recover from the pressure induced perturbations, as shown in Figure 7d. The electric field potentials and convection patterns changed significantly due to the sign change of the IMF B_Y. The Joule heating became slightly stronger in the dusk sector, but decreased significantly on the dawn. The ground magnetic perturbations were strongly negative with the exception of the high-latitude region ($> 70°$) located between 5-10 MLT. The negative perturbation peaked near the high-latitude midnight sector.

At 1450 UT, the dayside FAC profile did not show significant perturbations, however the electric field potentials in the nightside, especially in dusk region, were denser. The transient currents showed another pair of FACs with an opposite sense to the MI^- FACs. These FACs were likely to be ULF wave harmonics ((Shi et al., 2013), (Fujita et al., 2012)). Similar to previous cadence, the global Joule heating rate significantly decreased (blue shaded regions), but the weaker enhanced heating regions (shown in pink) associated with the PI^- and MI^- FACs propagated towards the midnight sector. Overall, the ground magnetic perturbation profile continued decreasing following the trend at 1445 UT.

Measurements from three magnetometer stations were selected and compared with the simulated magnetometer measurements to evaluate the fidelity of the simulation results. The locations of these magnetometers are shown in the bottom row of Figure 7. The magnetometers were chosen to sample the magnetic perturbation near 70° MLAT at dawn, noon and dusk. The comparison of the observations with the simulation results are shown in Figure 8. A 3-minute high-pass filter was applied to both the simulation results and the magnetometer observations to subtract the response to the background activity. The Hopen Island (HOP) magnetometer, located in the dusk sector at the time, recorded an enhancement lasting 5 minutes, followed by a 4 minute drop in the north (N) component of the magnetic field. The magnitude variation was not well captured by the simulated magnetometer. The drop in the simulated north component lasted longer in the simulated response. The Faroe Island (HOV) magnetometer recorded a slight 3-minute enhancement followed by a larger 4-minute drop in the magnetic field, which was captured by the model. This trend was opposite to the mid-latitude magnetometer behaviour reported in Ozturk et al. (2017) for local noon during SI^+s. The Rankin Inlet (RAN) magnetometer located in the dawn sector recorded a 4-minute drop followed by a 4-minute increase in the magnetic field. The responses of the HOV and RAN magnetometers to the magnetospheric expansion were well captured by the model however the simulation underestimated the magnitude of the perturbations, indicating the perturbations in the I-T system can be stronger than modeled. There was also a third response following the PI^- and MI^-, starting around 1448 UT at dawn and dusk sectors. This response was referred to as a second MI response by Fujita, Tanaka, and Motoba (2005) but this recovery response is beyond the scope of this paper. Overall, the trend of the dawn and dusk magnetometers were opposite of the Araki Model (Araki (1994a)) for a dynamic pressure enhancement event.

Figure 9 shows the ion convection, temperature and electron density variations from the GITM simulations, as a response to the sudden expansion of the magnetosphere. Figure 9a shows that the ion temperatures were below 1000 K everywhere before the event. The electron density at 210 km was depleted in regions with higher ion convection speeds, especially between 6-9 LT around 60° latitude. One minute after the start of the magnetospheric expansion, the ion temperature was enhanced over a very small area at 14.5 LT by around

This article is protected by copyright. All rights reserved.

Author Manuscript

Figure 7. The FACs, perturbation FACs, Joule heating profile and the simulated ground magnetometer responses to the solar wind dynamic pressure drop are shown for 1435 UT (a), 1438 UT (b), 1440 UT (c), 1445 UT (d) and 1450 UT (e). The numbers (1,2,3,4) show the perturbation FACs corresponding to magnetospheric flow perturbations. The green, blue and pink dots in the bottom panels show the locations of the HOP, HOV and RAN magnetometers.

This article is protected by copyright. All rights reserved.

Author Manuscript

Figure 8. The comparison of the simulated North component of the magnetic field perturbations (red) with HOP (a), HOV (b) and RAN (c) magnetometer measuremens (blue) are shown in between 1430 UT-1500 UT. The solid green line shows the response to solar wind dynamic pressure drop.

This article is protected by copyright. All rights reserved.

Author Manuscript

Figure 9. The GITM results for ion temperature and convection profiles at 210 km (top) and electron density (middle) are shown for 1435 UT (a), 1438 UT (b), 1440 UT (c), 1445 UT (d) and 1450 UT (e). The bottom panel shows the ion temperature for a meridional cut taken between 50° and 90° latitude at 11 LT, with horizontal ion convection velocities plotted on top for the same time steps. **P1** and **P2** show the location of ionospheric perturbations at 14.5 and 7.5 LTs respectively.

50 K (P1) associated with the upward PI^- FACs. The ion convection direction between 15-19 LT, around 70° latitude changed from east to equatorward, whereas the convection velocities dropped in the region between 5-9 LT, around 60° latitude. At 1440 UT, the hot patch (P1) associated with the upward PI^- FACs disappeared. The ion convection flows that previously changed direction between 15-19 LT, around 70° latitude became eastward. The weakened eastward flows in the region between 5-9 LT, around 60° latitude, became poleward as shown in the top panel of Figure 9c. At 1445 UT, the region between 5-9 LT (P2) was significantly heated due to the directional change in IMF B_Y. The ion temperature further increased at 1450 UT in Figure 9e when the convection flows in the hot spot B were clearly westward moving against the prevailing neutral wind. In the bottom row, the meridional cut of ion temperature at 7.5 LT showed a hot ion channel formation at 67° latitude, which was the center of the hot spot P2.

This article is protected by copyright. All rights reserved.

Author Manuscript

Figure 10a shows the ion, neutral, electron temperature and electron density profiles extracted from 66° latitude at the 14.5 LT, which corresponded to the perturbation shown as **P1**. The ion temperature profile change was small at this location, with the peak enhancement of 50 K occurring at 1438 UT between 240-300 km. The neutral temperature profile showed an enhancement by around 25 K between 1438 and 1440 UT, but the temperature dropped back to its initial values by 1445 UT. The electron temperature showed a significant increase of around 200 K at 1438 UT above 240 km due to the upward PI^- FAC, dropping back immediately afterwards. In addition, the electron density below 240 km was enhanced by 20% at this location. One possible reason for the spontaneous enhancement of electron temperature, and density are due to ionization and heating caused by the precipitating electrons (Schunk & Nagy, 2009) associated with the upward PI^- FACs over this location at 1438 UT.

Figure 10b shows the same profiles extracted from 67° latitude at the 7.5 LT, corresponding to the perturbation shown with **P2** in 9. The simulation results showed that the ion temperature was enhanced by around 150 K at 1445 UT and by around 175 K at 1450 UT around 180 km. The neutral temperature showed an insignificant enhancement at 1445 UT, which was around 2 K. However, at 1450 UT the neutral temperature decreased by around 10 K above 240 km. The electron temperature dropped at this location as a response to magnetospheric expansion, with the largest change occurring at 1450 UT, which was around 100 K above 240 km. Similarly, the electron density decreased below 210 km with the most significant drop, 50%, occurring below 120 km at 1450 UT, due to the FACs moving away from **P2**.

Figure 11a shows the ion and neutral East-West (E-W) velocities extracted from the perturbation labelled as **P1**. Both the ion and neutral velocities were westward before the event. The ion velocities became increasingly westward during the PI^- phase, however turned eastward during the MI^- phase. The peak difference occurred around 1438 UT, when ion convection vectors were enhanced further in the eastward direction due to the upward PI^- FAC. Figure 11b shows the same velocity profiles extracted from the location of the perturbation labelled as **P2**. Both the ion and neutral velocities were westward and significantly stronger than the velocities at **P1**. The ion velocity became increasingly eastward as the IMF B_Y changed sign. The reason for the large ion temperature increase seen at P2 in Figure 9 was this large difference between the ion and neutral velocities driving Joule heating.

4 Discussion and Conclusions

With the help of global and physics based simulations, the response of the geospace system to a sudden solar wind dynamic pressure decrease event has been investigated. During the expansion of the magnetosphere, the simulated magnetospheric flows showed interesting features, especially during the PI^- phase. One of the most comprehensive studies investigating the magnetospheric response to SI^-s was conducted by Zhao et al. (2016). They reported THEMIS-A observations of a counter clockwise rotating vortex in the dawn sector, and showed MHD simulation results of an oppositely rotating dawn-dusk vortex pair during the same time interval. The BATS-R-US MHD simulations reported above showed that immediately before to the vortices reported in Zhao et al. (2016), another set of vortices, the PI^- vortices, existed in the magnetosphere and their presence was verified with THEMIS-D velocity observations in the dusk sector. Simulations reported in Fujita et al. (2004) also showed sunward flows in the dayside magnetosphere during the PI^- phase, but the partial vortex profile (Fujita et al., 2004)] was not fully described, until the revisited study in Fujita et al. (2012). The source of the preliminary impulse during dynamic pressure enhancements was associated with the magnetopause boundary (Sibeck (1990), Kivelson and Southwood (1991), Keller et al. (2002), Fujita et al. (2003a), Samsonov et al. (2010), Yu and Ridley (2009), Tian et al. (2016)), however the proposed generation mechanisms differed. Samsonov et al. (2010) showed there are various different

This article is protected by copyright. All rights reserved.

Author Manuscript

Figure 10. The altitude profiles (110-500 km) of ion, neutral, and, electron temperature and electron density taken at 1435 UT (gray), 1438 (teal), 1440 UT (pink), 1445 UT (yellow) and 1450 UT (light green) for **P1** [7.5 LT, 67°] (a) and for **P2** [14.5 LT, 66°] (b) are shown.

This article is protected by copyright. All rights reserved.

Author Manuscript

Figure 11. The simulated ion (red) and neutral (blue) E-W velocities extracted from 7.5 LT at 67° associated with the perturbation labelled as **P1** (a) and 14.5 LT at 66° associated with the perturbation labelled as **P2** (b) are shown.

This article is protected by copyright. All rights reserved.

Author Manuscript

perturbations that can be generated during the compression of the magnetosphere. The propagation speed of these perturbations would depend on the magnetospheric conditions at the arrival time of the interplanetary shock. By employing an inner magnetospheric module, this study was able to demonstrate that magnetospheric return flows contribute to the vortex like flow perturbations in the magnetopause leading to the PI^- signatures. Furthermore, the measured ground magnetometer and simulated magnetic field responses in this study also indicated vortical structures through bipolar magnetic perturbation changes. The PI^- vortices were associated with an upward perturbation FAC in the dusk sector and a downward perturbation FAC in the dawn sector as shown in Figures 3 and 7. These FACs were responsible for the perturbations in the convection profiles which drove the Hall currents that caused a positive perturbation at dusk and a negative perturbation at dawn in the north component of the magnetic field.

The solar wind dynamic pressure dropped to a third of its previous value during the event reported in this study, which was lower than the 0.5 reported in Zhao et al. (2016) and 0.4 reported in Fujita et al. (2004). The formation and propagation of the magnetospheric vortices depended on the propagation speed of the fast magnetosonic wave (Sibeck (1990), Kivelson and Southwood (1991)). For the decompression event reported in this paper, the decompression front launched a fast magnetosonic wave through the magnetopause. A trough was formed due to the inward motion of the flank regions [x=$6R_E$, y=$\pm 6R_E$] while the magnetopause nose radially expanded outward [x=8-$10R_E$, y=$0R_E$]. The magnetosphere continued expanding behind the solar wind discontinuity with a speed close to 90 km/s, until it reached to a pressure balance with the solar wind. The first set of magnetospheric vortices reported in this paper in association with the PI^- signatures, formed as a result of the magnetopause boundary motion in which the boundary moved (i) inward, due to the propagation of the trough, (ii) sunward, due to the return flows in the magnetosphere and (iii) outward, due to the propagation of the ridge, creating a counter clock-wise rotating vortex at dusk and a clock-wise rotating vortex at dawn. The second set of magnetospheric vortices in association with the MI^- signatures, occurred as a result of: (i) the outward motion due to the passage of the ridge, (ii) the sunward and (iii) the tailward flows due to the pressure gradients, forming a clock-wise rotating vortex at dusk and a counter clock-wise rotating vortex at dawn. The trough (T) and ridge (R) can be seen clearly at Figures 4b and c as the trough propagated from x=-23 R_E to x=-40 R_E in 5 minutes whereas the trailing ridge amplitude grew. The generation mechanism for the magnetospheric vortices was attributed to the Kelvin-Helmholtz instability by Fujita et al. (2012).

The north component of the magnetic field perturbations on the ground, derived by virtual magnetometers, showed only slight deviations from the Araki model of SI^-s (Araki & Nagano, 1988). The perturbations associated with the PI^- phase between 1436 UT and 1440 UT, showed an enhancement in the low-latitude dawn sector and high-latitude noon and midnight sectors. The MI^- phase perturbations from 1440 UT onwards, were mostly negative with strong dips in the low-latitude noon and high-latitude midnight sectors. One exception to the overall negative trend was seen at the high-latitude noon sector, but with lower magnitudes than that of the negative dips. These differences from the Araki model can be attributed to various conditions such as solar EUV driven conductance patterns, which results in asymmetric distribution of the FACs between dayside and the nightside. Another reason can be the large and fluctuating IMF B_Y variations that introduce dawn-dusk asymmetries in the FAC profiles that in return determine the magnetic perturbations at the ground level. As this study showed, the superpositions of the magnetospheric perturbation flows and ionospheric perturbation currents on the pre-existing profiles are extremely important in understanding the effects of such transients on the M-I-T system. Therefore another reason for not observing an exact mirror image of SI^+ responses in the N-component of magnetic field perturbations, could be due to the conditions of the pre-existing magnetosphere and ionosphere systems.

This article is protected by copyright. All rights reserved.

Author Manuscript

The ion convection flows and auroral signatures resulting from the sudden drop in the solar wind dynamic pressure altered the density and temperature profiles in the I-T system. These perturbations were further investigated using GITM with the electric field potentials and particle flux from MHD model. The Joule heating increased in a short-lived manner in regions sandwiched by the perturbation FACs, which results in an ion temperature increase by 50 K. Overall, the I-T system response to magnetospheric expansion showed a clear dawn-dusk asymmetry. The IMF B_Y changed sign during this event, causing the convection flows to change their direction from closely aligned with the neutral wind to its opposite direction. This direction change led to an increased frictional heating between ions and neutrals, causing the hot spot **P2** seen in the morning sector, where the ion temperature increased by around 150 K.

This case study of the solar wind dynamic pressure decrease on 11 June 2017 revealed interesting magnetospheric flow profiles that were not evident in previous studies. Although this case was very useful in portraying the global response to a solar wind dynamic pressure decrease event, it also shows how helpful idealized simulations can be in understanding isolated effects of the solar wind drivers on the M-I-T system.

The geospace system response to the solar wind dynamic pressure decrease on 11 June 2017, between 1430-1500 UT, was studied using BATS-R-US and GITM simulations as well as in situ spacecraft and ground magnetometer observations. The electric field potential and particle precipitation profiles derived from the magnetospheric simulations were used to drive GITM. The main results of this study can be summarized as follows:

1. The dayside magnetosphere rapidly expanded sunward after the pressure decrease.
2. A pair of dawn-dusk vortices appeared at the dayside flanks as a response to magnetospheric expansion. These PI^- vortices had a counter clockwise sense of rotation at dusk, and a clockwise sense of rotation at dawn.
3. Another pair of dawn-dusk vortices formed inside the magnetosphere following the PI^- vortices. These MI^- vortices had a clockwise sense of rotation at dusk and a counter clockwise sense of rotation at dawn.
4. These vortices mapped to the ionosphere as PI^- FACs (downward on dawn and upward on dusk) and MI^- FACs (upward on dawn and downward on dusk).
5. The peak Joule heating in the I-T system occurred between the perturbation FACs on the dayside driving an ion temperature increase by around 50 K in the afternoon sector. The IMF B_Y sign change in this case led to a change in the direction of the convection flow and an enhancement of 150 K in the ion temperature.
6. The polarity distribution of the magnetic field perturbations at the ground level slightly deviated from the SI^- model of Araki (1994a), which is a mirror image of the SI^+, but this deviation is likely due to the variations in the IMF B_Y, but further idealized simulation studies are needed.

Acknowledgments

The authors would like to gratefully acknowledge the high-performance computing support from Cheyenne (doi:10.5065/D6RX99HX) provided by National Center for Atmospheric Research (NCAR) Computational and Information Systems Laboratory, sponsored by the National Science Foundation, the University of Michigan Center for Space Environment Modeling and the SpacePy Team. The work was supported by NSF Grant no: AGS1400998 and J. A. Slavin was supported by NASA MMS GI grant F05043. The research has made use of NASA's Astrophysics Data System. Portions of this work were done at the Jet Propulsion Laboratory, California Institute of Technology, under a contract with NASA. For the ground magnetometer data, we gratefully acknowledge: SuperMAG, PI Jesper W. Gjerloev, for the THEMIS Mission data, we want to acknowledge: NASA contract NAS5-02099 and V. Angelopoulos, C.W. Carlson and J. P. McFadden, for the MMS Mission data, we would like to acknowledge Dr. Roy Torbert the lead Co-I of the FIELDS instrument

This article is protected by copyright. All rights reserved.

Author Manuscript

suite, and Dr. C. T. Russell, the PI of the FGM instrument and the MMS team for their efforts to make data available to the public through the MMS Science Data Center website (https://lasp.colorado.edu/mms/sdc/public/). In addition the use of NASA/GSFC's Space Physics Data Facility's OMNIWeb (or CDAWeb or ftp) service, and OMNI data is acknowledged. Authors appreciate the valuable comments by the reviewers. D. S. Ozturk thanks to Olga Verkhoglyadova for the insightful sugggestions. The simulation results can be found on the University of Michigan DeepBlue Data Repository with doi:10.7302/Z26T0JW6.

References

Araki, T. (1994a). Global structure of geomagnetic sudden commencement. *Planetary Space Science*, *25, 373-384*. doi: https://doi.org/10.1016/0032-0633(77)90053-8

Araki, T. (1994b). A physical model of geomagnetic sudden commencement. *AGU*, *81*. doi: https://doi.org/10.1029/GM081p0183

Araki, T., & Nagano, H. (1988). Geomagnetic response to sudden expansion of the magnetosphere. *Journal of Geophysical Research*. doi: https://doi.org/10.1029/JA093iA05p03983

Belakhovsky, V. B., & Vorobjev, V. G. (2016). Response of the night aurora to a negative sudden impulse. *Geomagnetism and Aeronomy*. doi: https://doi.org/10.1134/S0016793216060037

Fujita, S., Tanaka, T., Kikuchi, T., Fujimoto, K., Hosokawa, K., & Itonaga, M. (2003a). A numerical simulation of the geomagnetic sudden commencement: 1. generation of the field-aligned current associated with the preliminary impulse. *Journal of Geophysical Research*. doi: https://doi.org/10.1029/2002JA009407

Fujita, S., Tanaka, T., Kikuchi, T., Fujimoto, K., & Itonaga, M. (2003b). A numerical simulation of the geomagnetic sudden commencement: 1. plasma processes in the main impulse. *Journal of Geophysical Research*. doi: https://doi.org/10.1029/2002JA009763

Fujita, S., Tanaka, T., Kikuchi, T., & Tsunomura, S. (2004). A numerical simulation of a negative sudden impulse. *Earth Planets Space*. doi: https://doi.org/10.1186/BF03352499

Fujita, S., Tanaka, T., & Motoba, T. (2005). A numerical simulation of the geomagnetic sudden commencement: 3. a sudden commencement in the magnetosphere-ionosphere compound system. *Journal of Geophysical Research*. doi: https://doi.org/10.1029/2005JA011055

Fujita, S., Yamagishi, H., Murata, K. T., Den, M., & Tanaka, T. (2012). A numerical simulation of a negative solar wind impulse: Revisited. *Journal of Geophysical Research*. doi: https://doi.org/10.1029/2012JA017526

Garcia, K. S., & Hughes, W. J. (2007). Finding the lyon-fedder-mobarry magnetopause: A statistical perspective. *Journal of Geophysical Research*. doi: https://doi.org/10.1029/2006JA012039

Kataoka, R., Fukunishi, H., Fujita, S., Tanaka, T., & Itonaga, M. (2004). Transient response of the earth's magnetosphere to a localized density pulse in the solar wind: Simulation of traveling convection vortices. *Journal of Geophysical Research*. doi: https://doi.org/10.1029/2003JA010287

Keller, K. A., Hesse, M., Kuznetsova, M., Rastätter, L., Moretto, T., Gombosi, T. I., & DeZeeuw, D. L. (2002). Global mhd. modeling of the impact of a solar wind pressure change. *Journal of Geophysical Research: Space Physics*. doi: https://doi.org/10.1029/2001JA000060

Kivelson, M. G., & Southwood, D. J. (1991). Ionospheric traveling convection vortex generation by solar wind buffeting of the magnetosphere. *Journal of Geophysical Research*. doi: https://doi.org/10.1029/90JA01805

Liou, K. (2007). Large, abrupt pressure decreases as a substorm onset trigger. *Geophysical Research Letters*, *34*. doi: https://doi.org/10.1029/2007GL029909

Newell, P. T., Sotirelis, T., Ruohoniemi, J. M., Carbary, J. F., Liou, K., Skura, J. P., ... Rich, F. J. (2002). Ovation: Oval variation, assesment, tracking, intensity and online

This article is protected by copyright. All rights reserved.

Author Manuscript

nowcasting. *Annales Geophysicae*. doi: https://doi.org/10.5194/angeo-20-1039-2002

Ozturk, D. S., Zou, S., Ridley, A. J., & Slavin, J. A. (2018). Modeling study of the geospace system response to the solar wind dynamic pressure enhancement on 17 march 2015. *Journal of Geophysical Research: Space Physics*. doi: https://doi.org/10.1002/2017JA025099

Ozturk, D. S., Zou, S., & Slavin, J. A. (2017). Imf by effects on ground magnetometer response to increased solar wind dynamic pressure derived from global mhd simulations. *Journal of Geophysical Research*. doi: https://doi.org/10.1002/2017JA023903

Ridley, A. J., Gombosi, T. I., & DeZeeuw, D. L. (2004). Ionospheric control of the magnetosphere: conductance. *Annales Geophysicae*, *22*, 567-584. doi: https://doi.org/10.5194/angeo-22-567-2004

Samsonov, A. A., Nemecek, Z., & Safrankova, J. (2006). Numerical mhd modeling of propagation of interplanetary shock through the magnetosheath. *Journal of Geophysical Research*. doi: https://doi.org/10.1029/2005JA011537

Samsonov, A. A., & Sibeck, D. G. (2013). Large-scale flow vortices following a magnetospheric sudden impulse. *Journal of Geophysical Research*. doi: https://doi.org/10.1002/jgra.50329

Samsonov, A. A., Sibeck, D. G., & Yu, Y. (2010). Transient changes in magnetospheric-ionospheric currents caused by the passage of an interplanetary shock: Northward interplanetary magnetic field case. *Journal of Geophysical Research*. doi: https://doi.org/10.1029/2009JA014751

Sato, N., Murata, Y., Yamagishi, H., Yukimatu, A. S., Kikuchi, M., Watanabe, M., ... Rich, F. J. (2001). Enhancement of optical aurora triggered by the solar wind negative pressure impulse. *Geophysical Research Letters*, *28*(1), 127-130. doi: https://doi.org/10.1029/2000GL003742

Schunk, R., & Nagy, A. (2009). *Ionospheres physics, plasma physics and chemistry*. Cambridge University Press.

Shi, Q. Q., Hartinger, M. D., Angelopoulos, V., Tian, A. M., Fu, S. Y., Zong, Q.-G., ... Shen, X. C. (2013). Solar wind pressure pulse-driven magnetospheric vortices and their global consequences. *Journal of Geophysical Research: Space Physics*. doi: https://doi.org/10.1002/2013JA019551

Sibeck, D. G. (1990). A model for the transient magnetospheric response to sudden solar wind dynamic pressure variations. *Journal of Geophysical Research*. doi: https://doi.org/10.1029/JA095iA04p03755

Sun, T. R., Wang, C., Zhang, J. J., Pilipenko, V. A., Wang, Y., & Wang, J. Y. (2014). The chain response of the magnetospheric and ground mangetic field to interplanetary shocks. *Journal of Geophysical Research*. doi: https://doi.org/10.1002/2014JA020754

Takeuchi, T., Araki, T., Luehr, H., Rasmussen, O., Watermann, J., Milling, D. K., ... Nagai, T. (2000). Geomagnetic negative sudden impulse due to a magnetic cloud observed on may 13, 1995. *Journal of Geophysical Research*, *105*(A8), 18835-18846. doi: https://doi.org/10.1029/2000JA900055

Takeuchi, T., Araki, T., Viljanen, A., & Watermann, J. (2002). Geomagnetic negative sudden impulses: Interplanetary causes and polarization distribution. *Journal of Geophysical Research*, *107*(A7). doi: https://doi.org/10.1029/2000JA900055

Tamao, T. (1965). *Transmission and coupling resonance of hydromagnetic disturbances in the non-uniform earth's magnetosphere* (Tech. Rep.).

Thayer, J. P., Vickrey, J. F., Heelis, R. A., & Gary, J. B. (1995). Interpretation and modeling of high-latitude electromagnetic energy flux. *Journal of Geophysical Research*. doi: https://doi.org/10.1029/95JA01159

Tian, A. M., Shen, X. C., Shi, Q. Q., Tang, B. B., Nowada, M., Zong, Q. G., & Fu, S. Y. (2016). Dayside magnetospheric and ionospheric responses to solar wind pressure increase: Multispacecraft and ground observations. *Journal of Geophysical Research: Space Physics*. doi: https://doi.org/10.1002/2016JA022459

Toffoletto, F., Sazykin, S., Spiro, R., & Wolf, R. (2003). Inner magnetospheric modeling

This article is protected by copyright. All rights reserved.

with the rice convection model. *Space Science Reviews*, *107*, 175-196. doi: https://doi.org/10.1023/A:1025532008047

Toth, G., Sokolov, I. V., Gombosi, T. I., Chesney, D. R., Clauer, C. R., DeZeeuw, D. L., ... Yu, B. (2005). Space weather modeling framework: A new tool for the space science community. *Journal of Geophysical Research*. doi: https://doi.org/10.1029/2005JA011126

Weimer, D. R. (2005). Predicting surface geomagnetic variations using ionospheric electrodynamic models. *Journal of Geophysical Research*. doi: https://doi.org/10.1029/2005JA011270

Yu, Y., & Ridley, A. J. (2009). The response of the magnetosphere-ionosphere system to a sudden dynamic pressure enhancement under southward imf conditions. *Annales Geophysicae*. doi: https://doi.org/10.5194/angeo-27-4391-2009

Yu., Y., & Ridley, A. J. (2011). Understanding the response of the ionosphere-magnetosphere system to sudden solar wind density increases. *Journal of Geophysical Research*. doi: https://doi.org/10.1029/2010JA015871

Zhang, X. Y., Zong, Q. G., Wang, Y. F., Zhang, H., Xie, L., Fu, S. Y., ... Pu, Z. Y. (2010). Ulf waves excited by negative/positive solar wind dynamic pressure impulses at geosynchronous orbit. *Journal of Computational Physics*. doi: https://doi.org/10.1029/2009JA015016

Zhao, H. Y., Shen, X. C., Tang, B. B., Tian, A. M., Shi, Q. Q., Weygand, J. M., ... Pu, Z. Y. (2016). Magnetospheric vortices and their global effect after a solar wind dynamic pressure decrease. *Journal of Geophysical Research: Space Physics*, *121*, 1071-1077. doi: https://doi.org/10.1002/2015JA021646

Zhou, X., & Tsuratani, B. T. (1999). Rapid intensification and propagation of the dayside aurora: Large scale interplanetary pressure pulses (fast shocks). *Geophysical Research Letters*. doi: https://doi.org/10.1029/1999GL900173

Author Manuscript

This article is protected by copyright. All rights reserved.

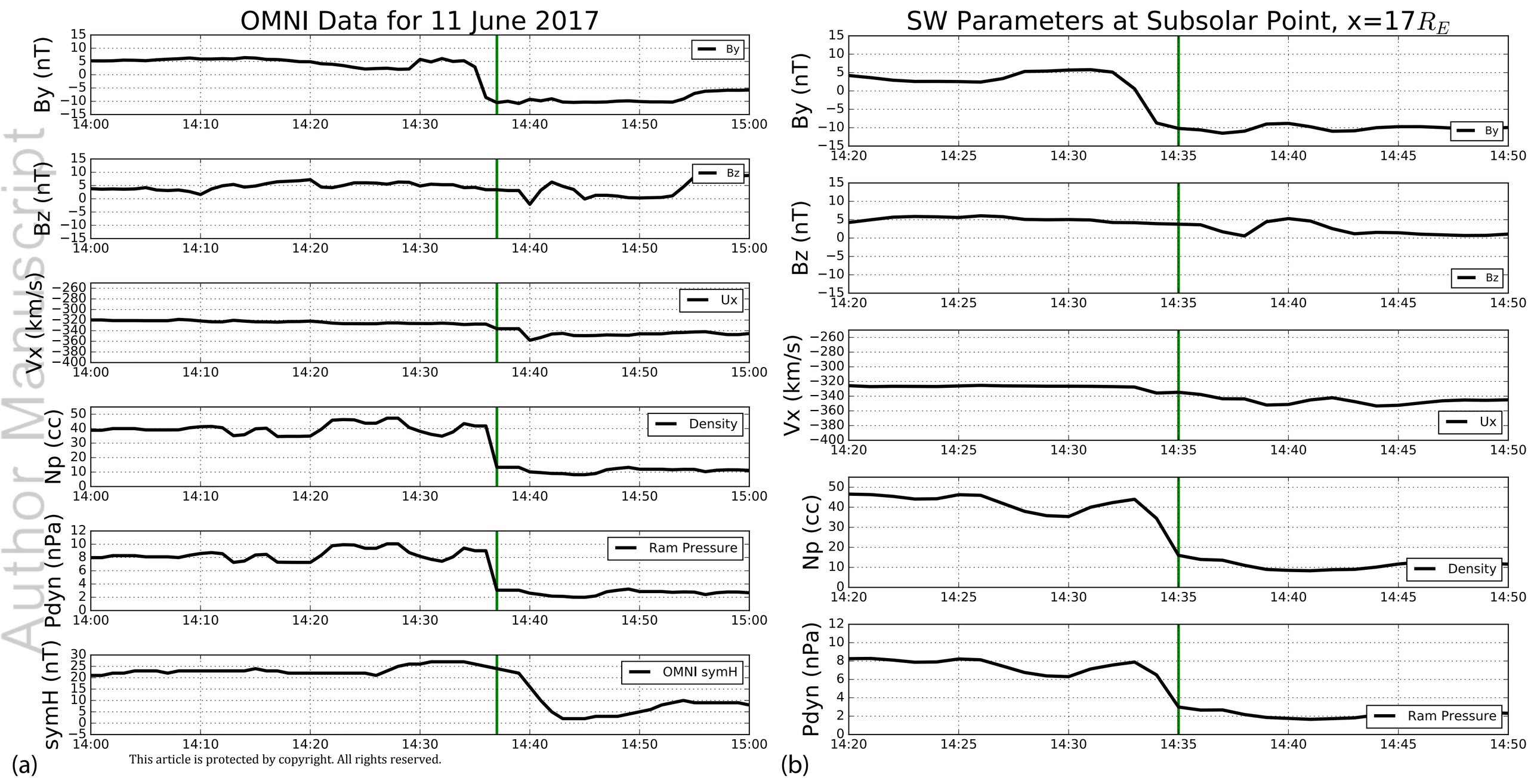

Author Manuscript

This article is protected by copyright. All rights reserved.

Author Manuscript

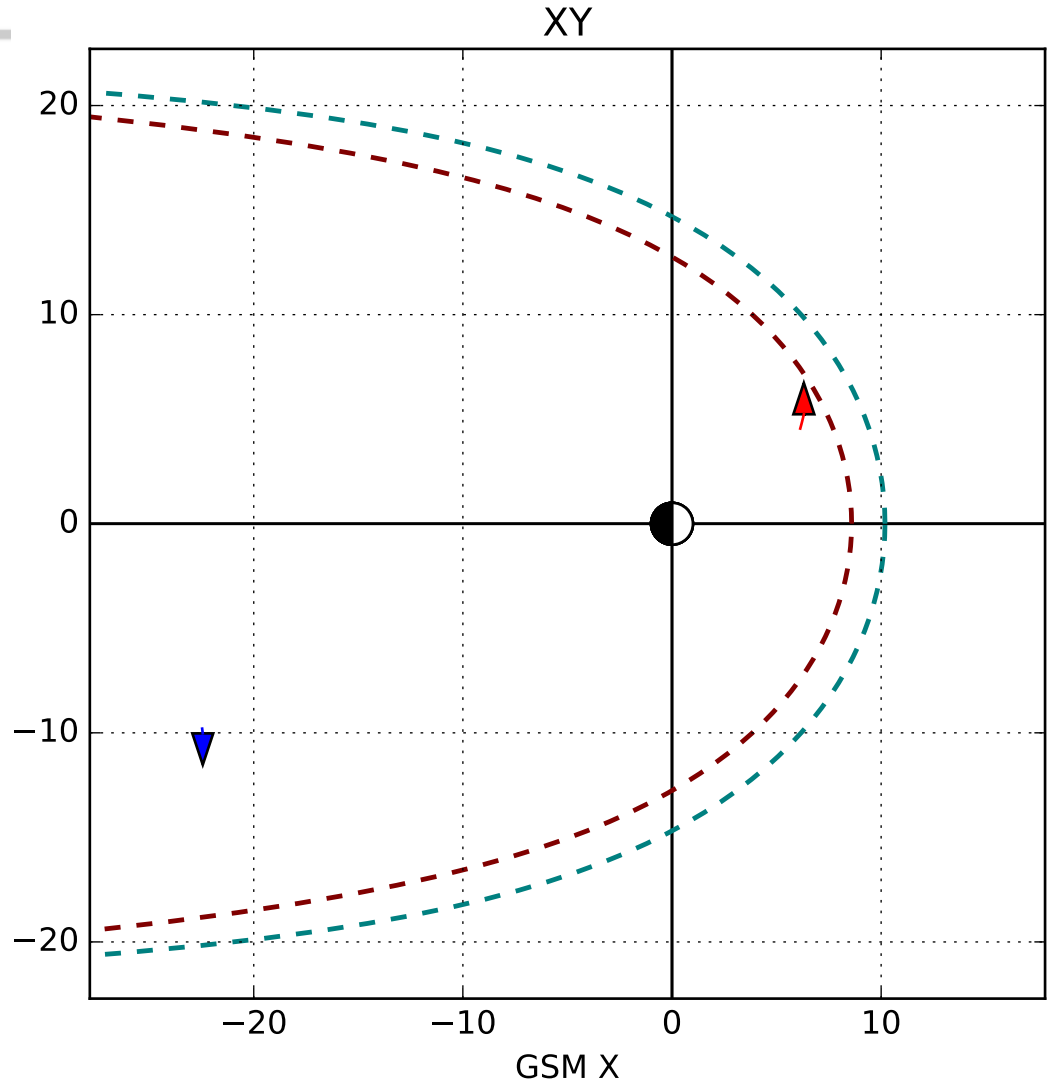

(a)

This article is protected by copyright. All rights reserved.

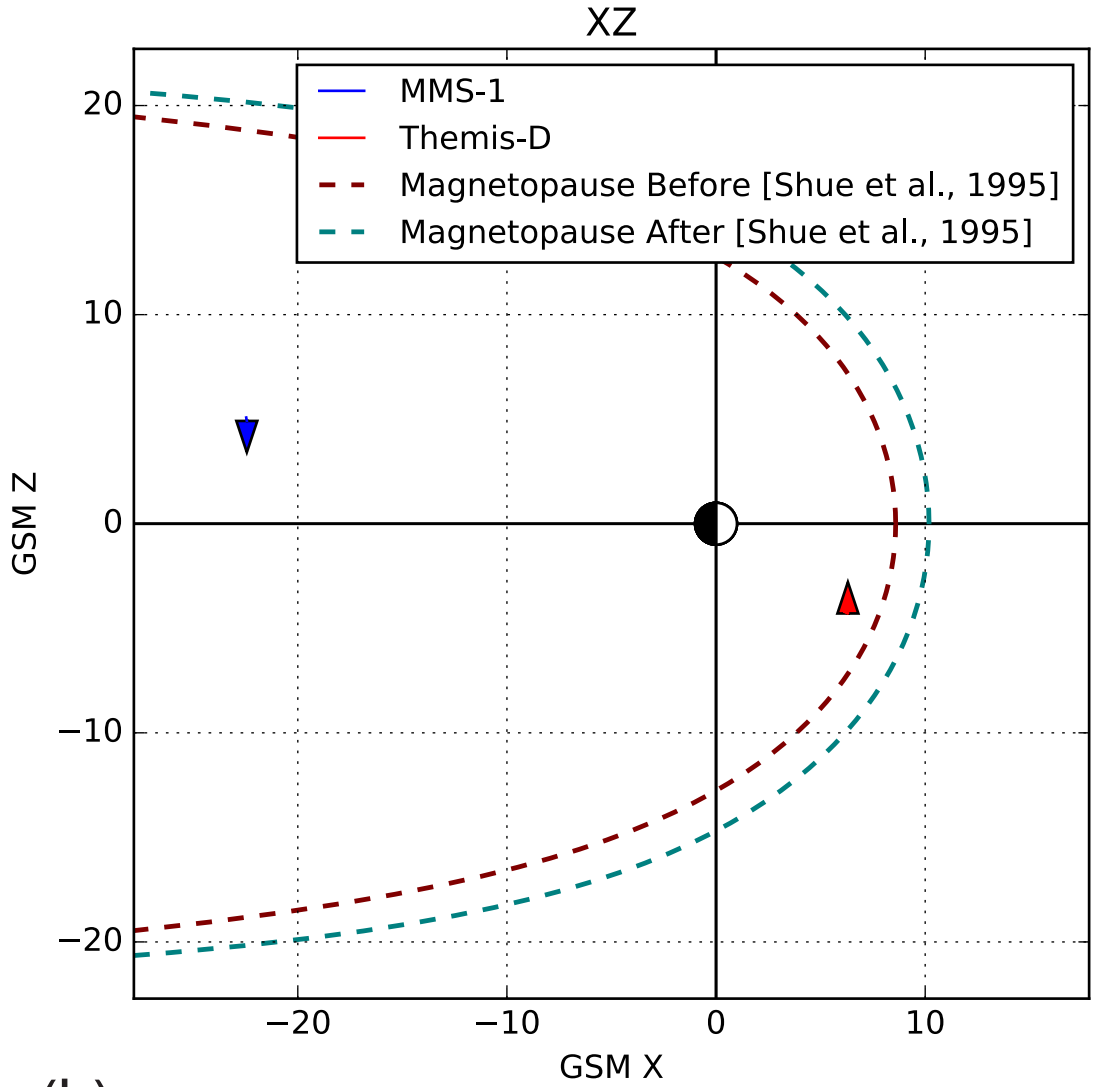

(b)

Author Manuscript

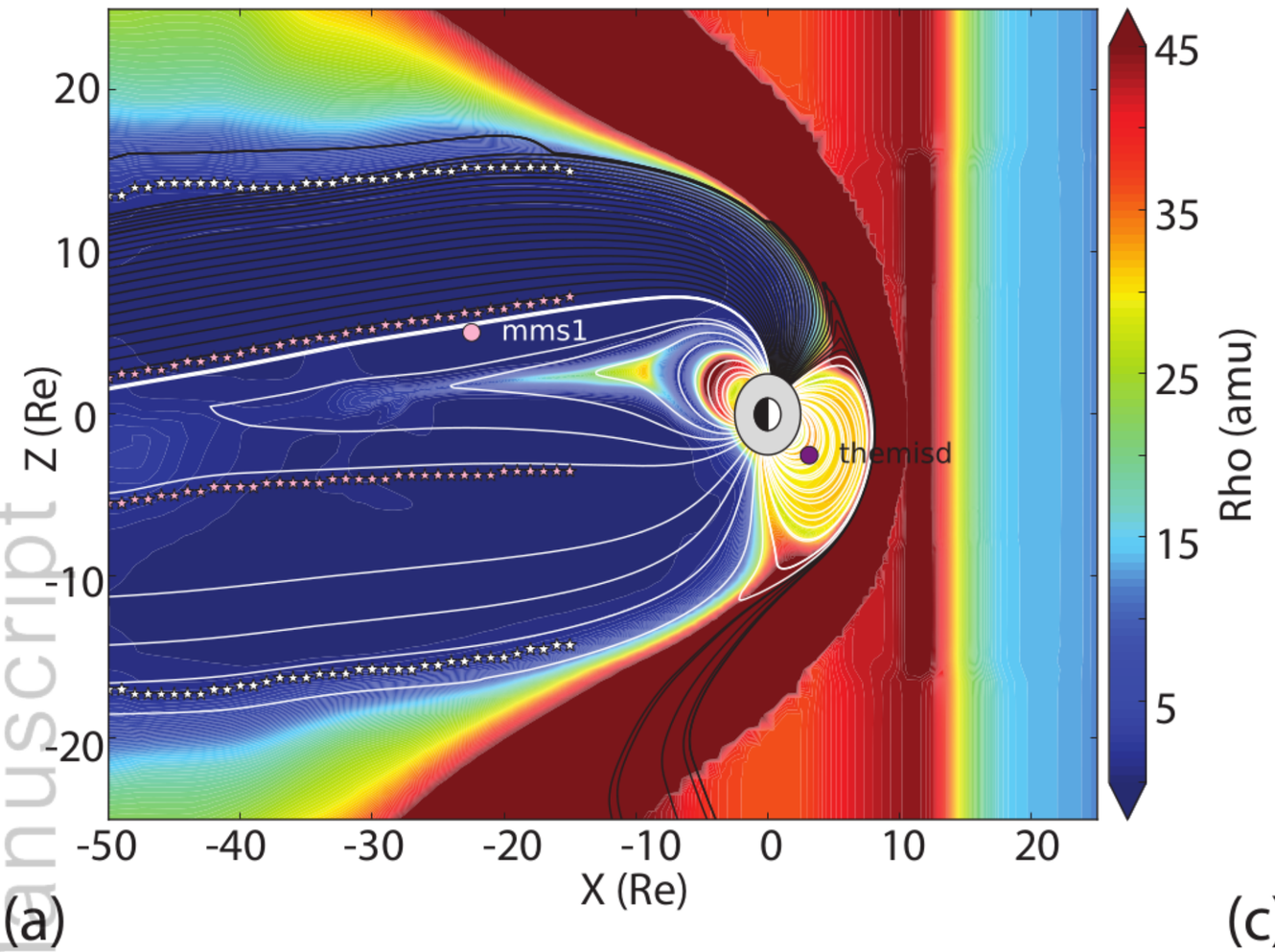

(a)

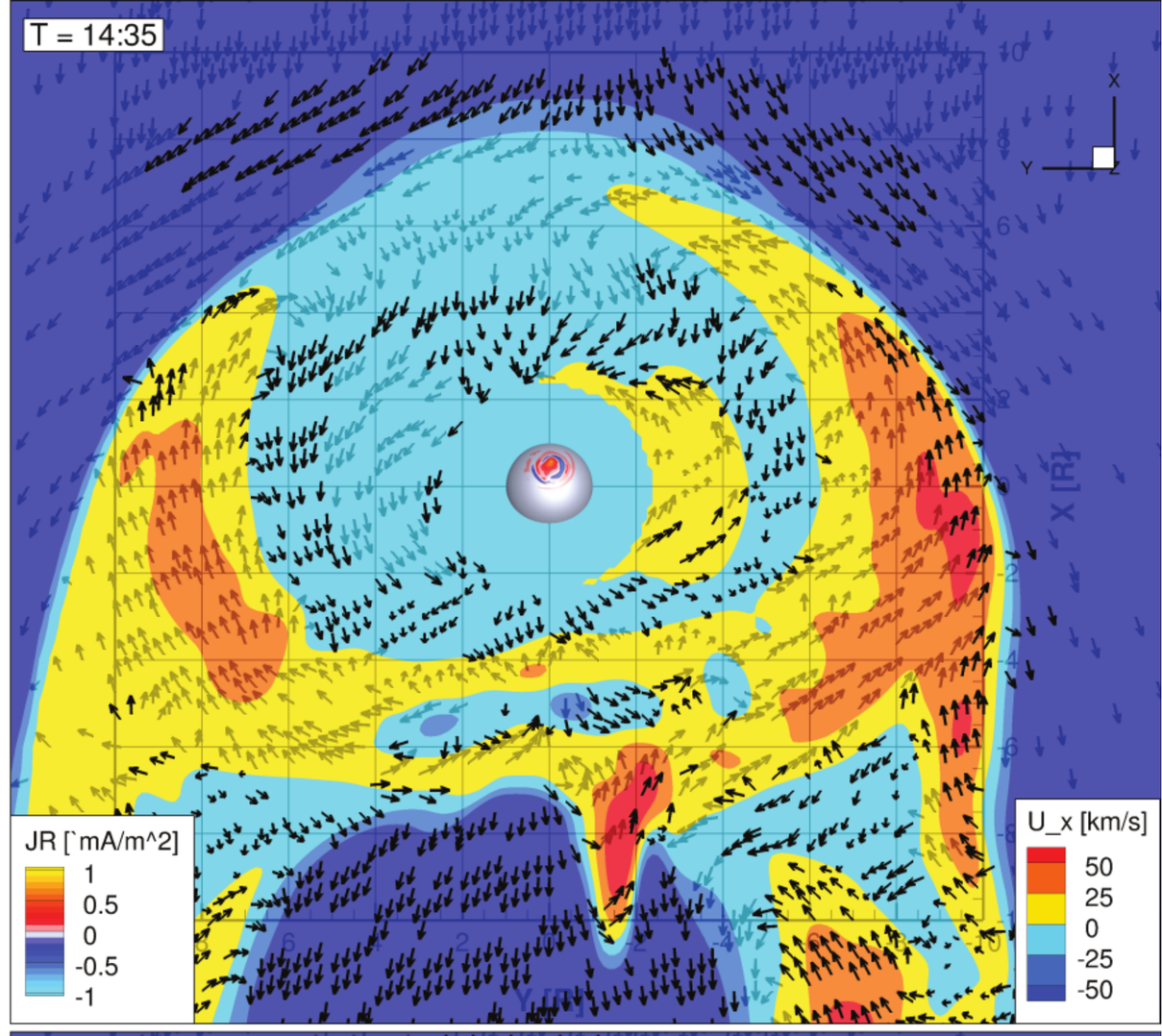

(c)

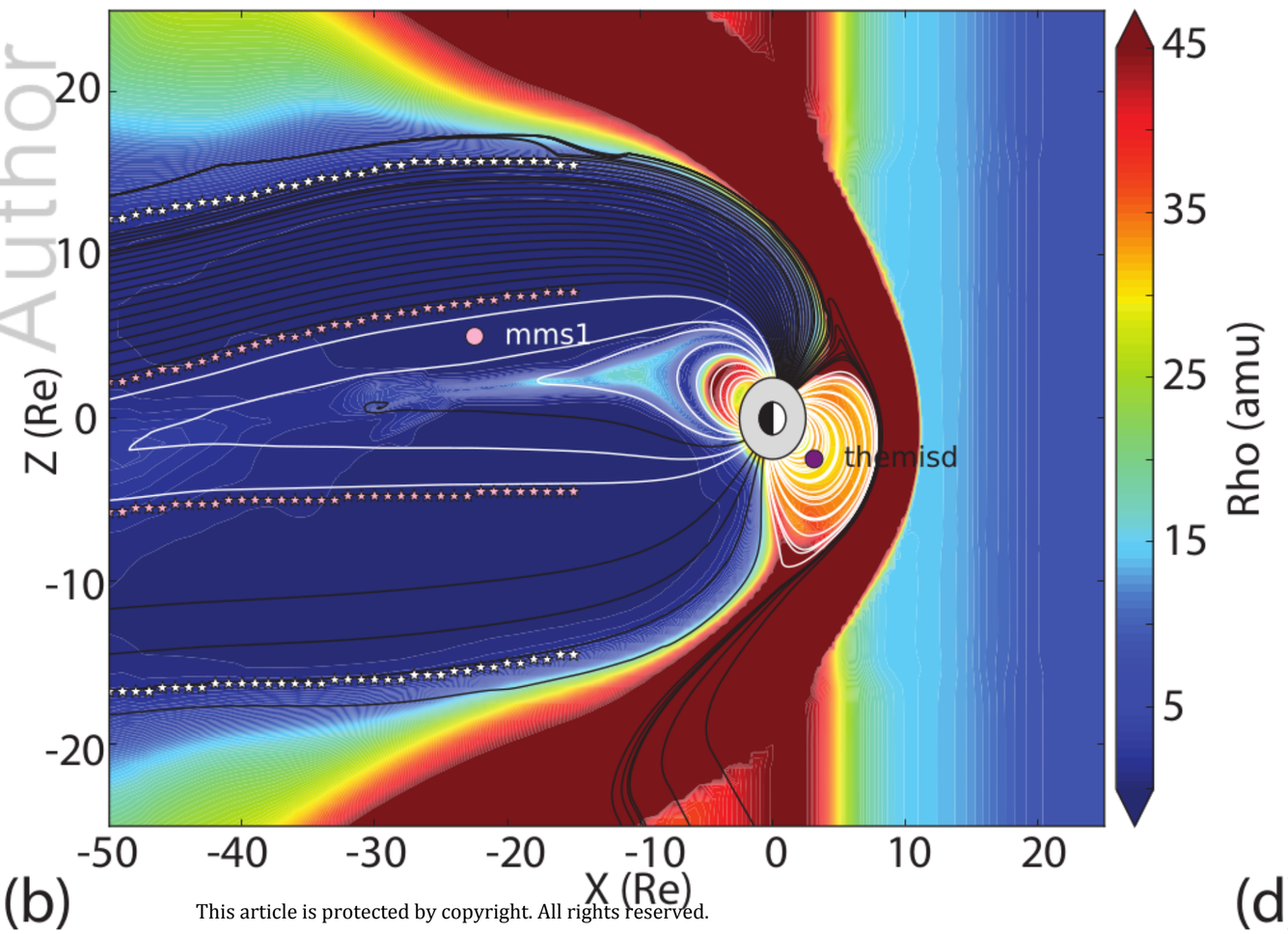

(b)

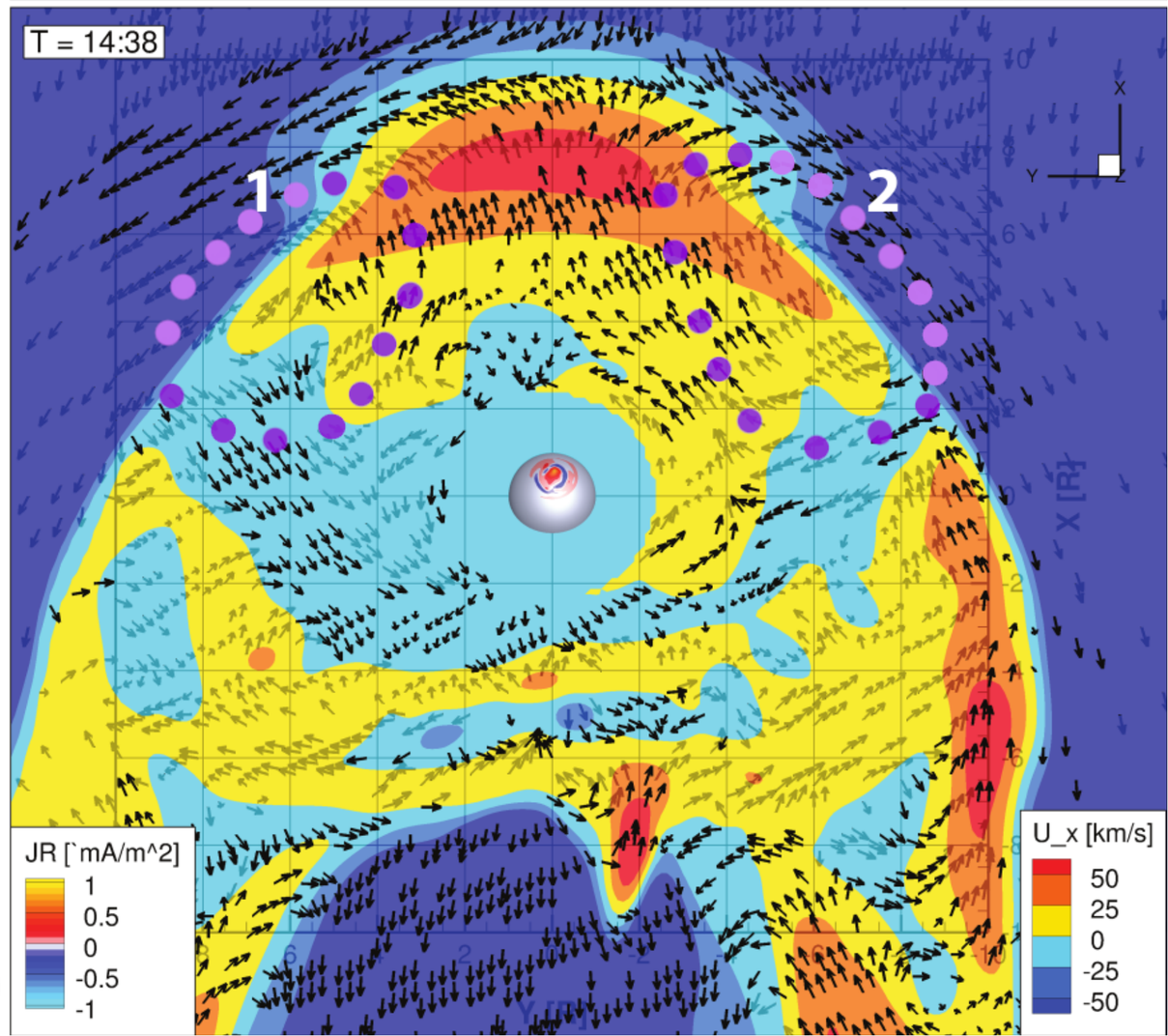

(d)

This article is protected by copyright. All rights reserved.

Author Manuscript

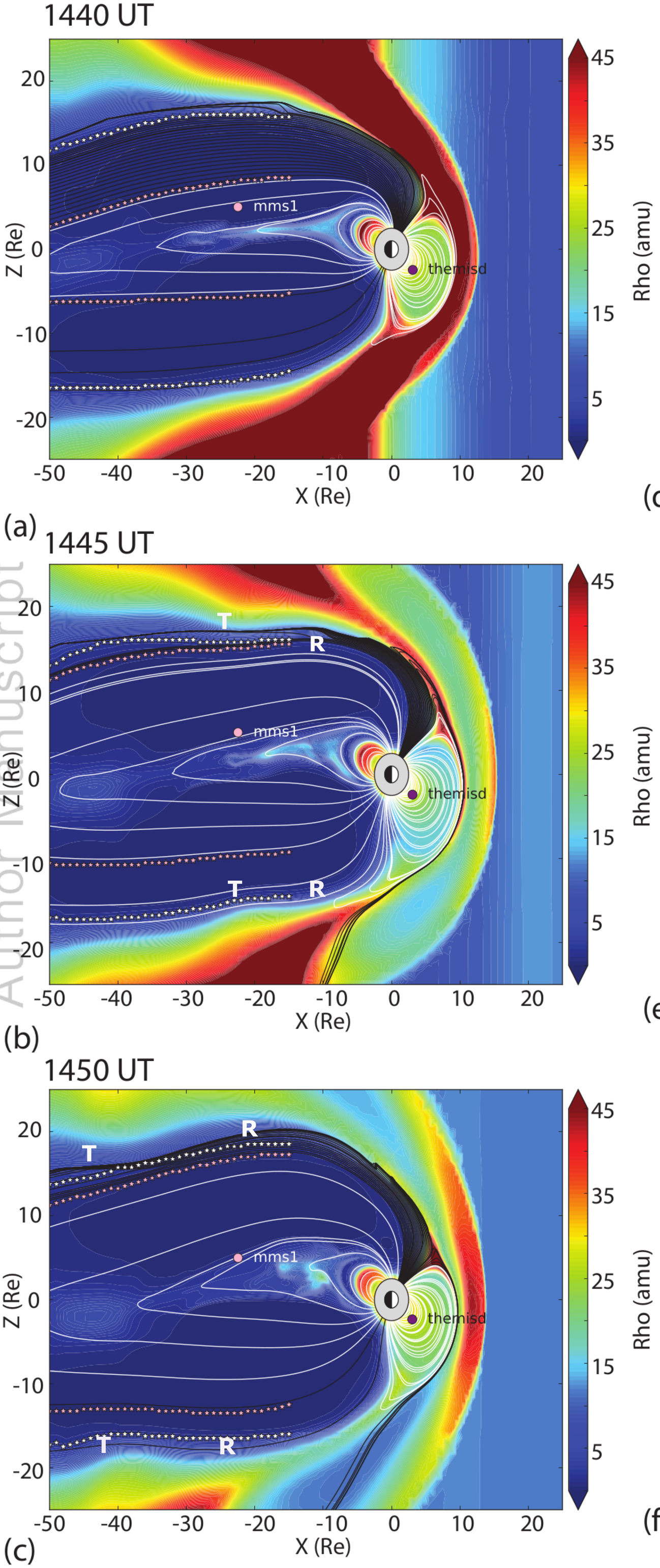

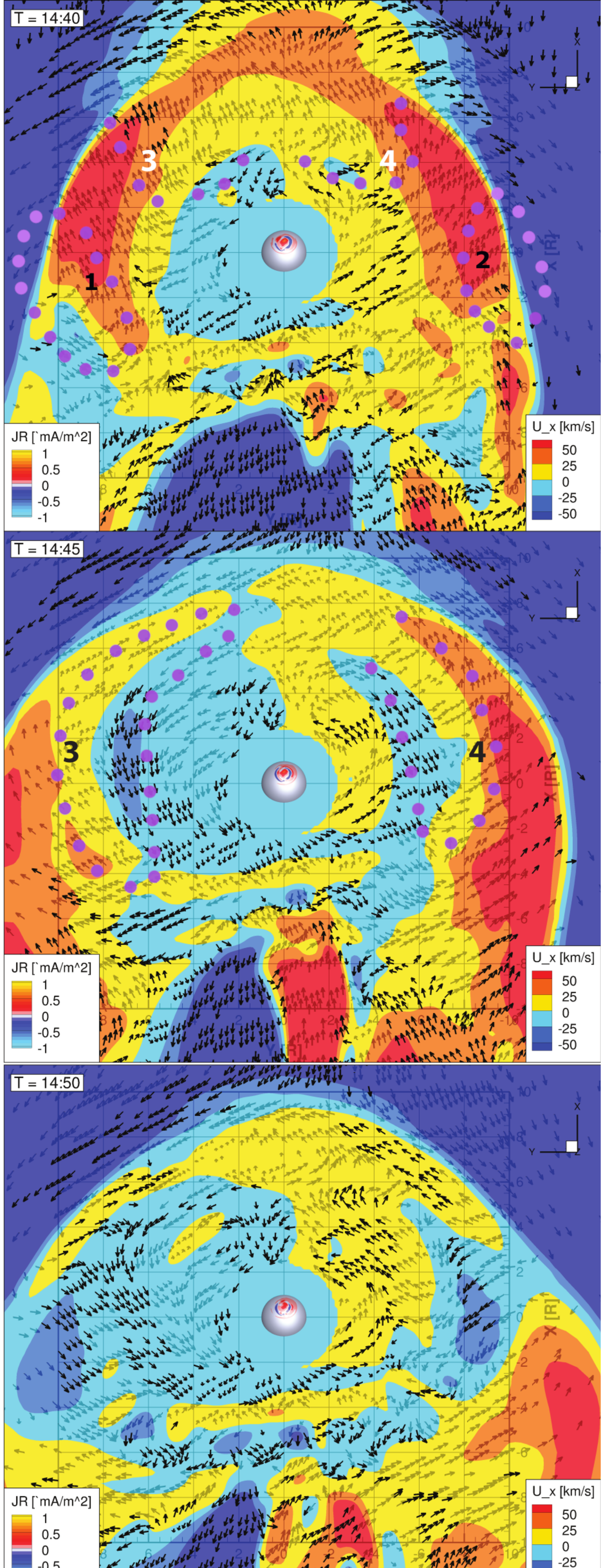

This article is protected by copyright. All rights reserved.

Author Manuscript

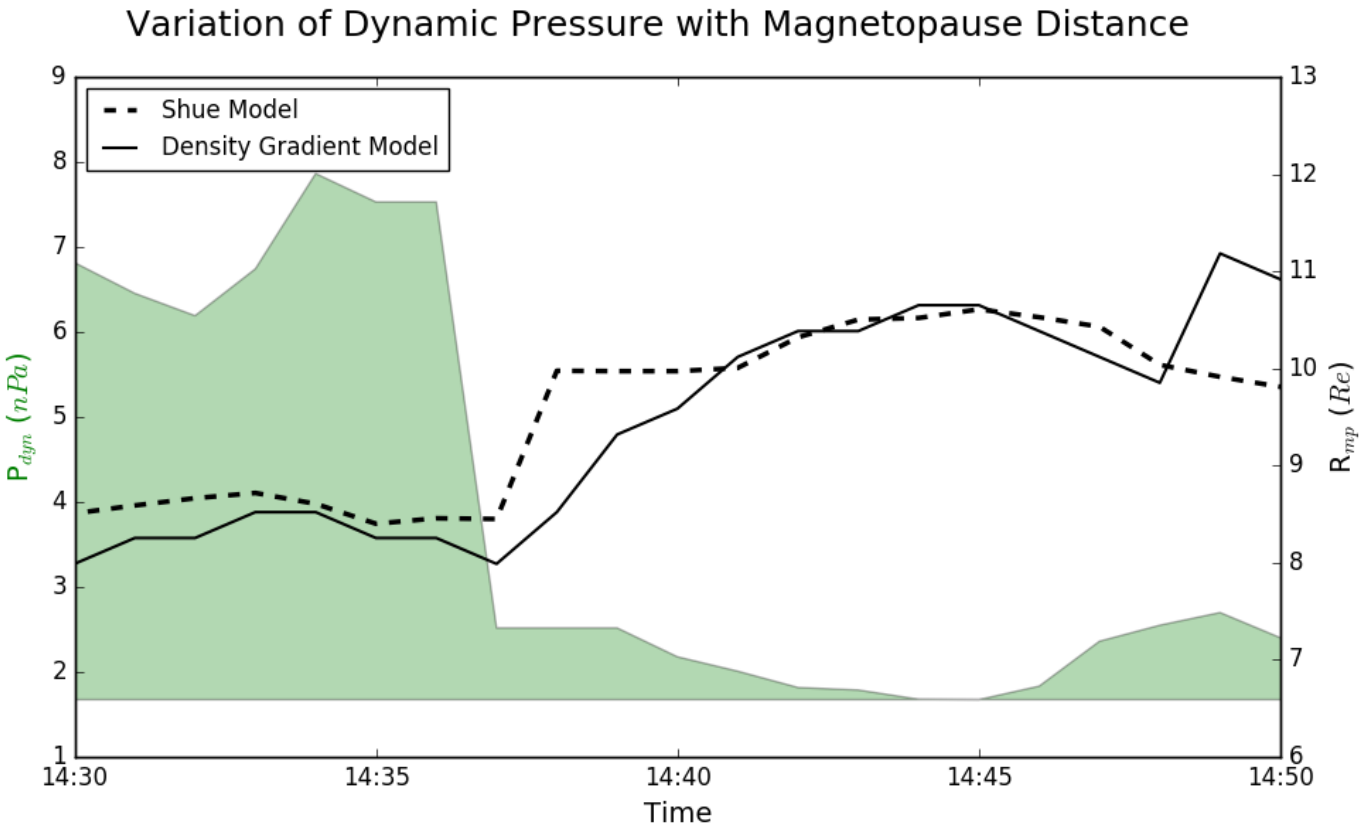

2018JA026315-f05-z-.png

This article is protected by copyright. All rights reserved.

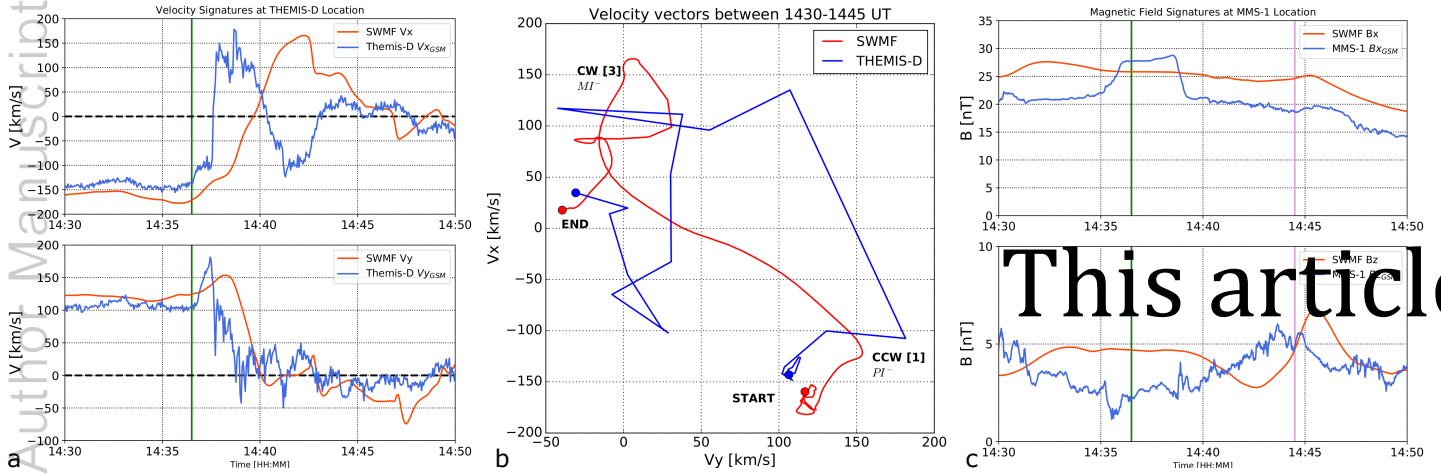

Author Manuscript

This article

Author Manuscript

1435 UT | 1438 UT | 1440 UT | 1445 UT | 1450 UT

FACs

Diff FACs

Joule Heating

Magnetic Perturbations

(a) (b) (c) (d) (e)

This article is protected by copyright. All rights reserved.

Author Manuscript

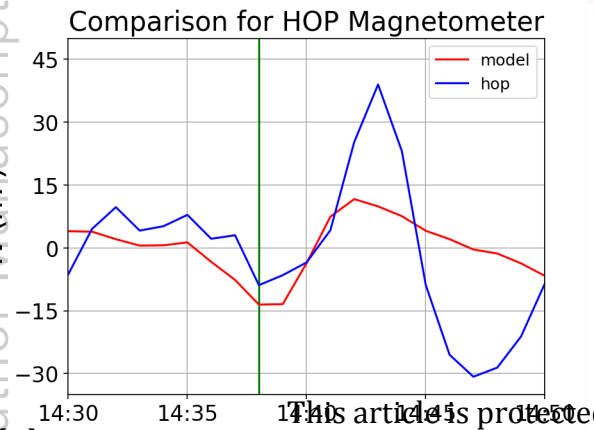

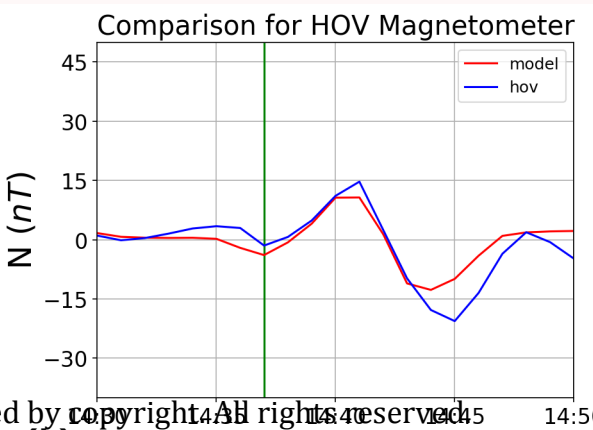

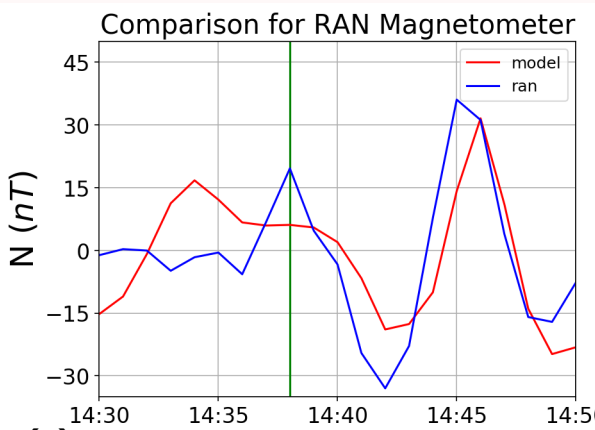

This article is protected by copyright. All rights reserved.

Author Manuscript

1435 UT | 1438 UT | 1440 UT | 1445 UT | 1450 UT

Global Ion Temperature

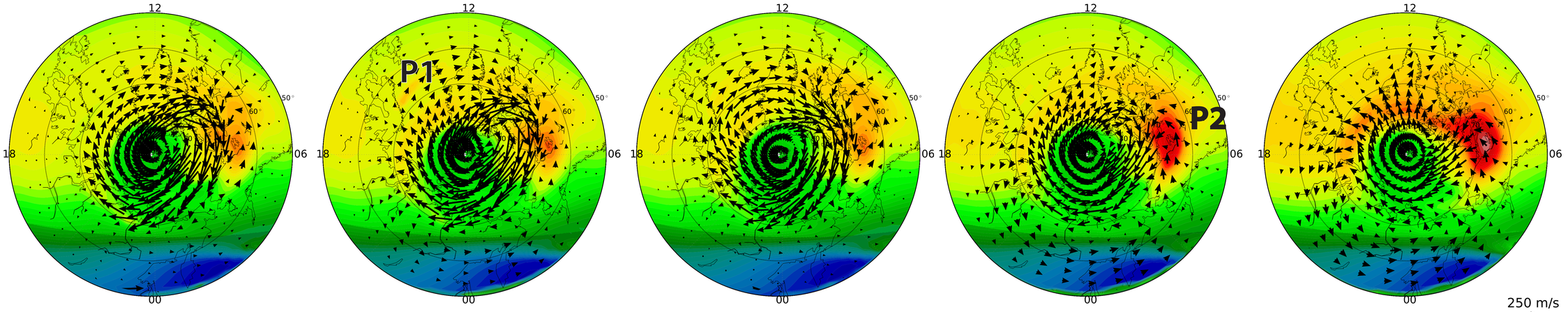

Global Electron Density

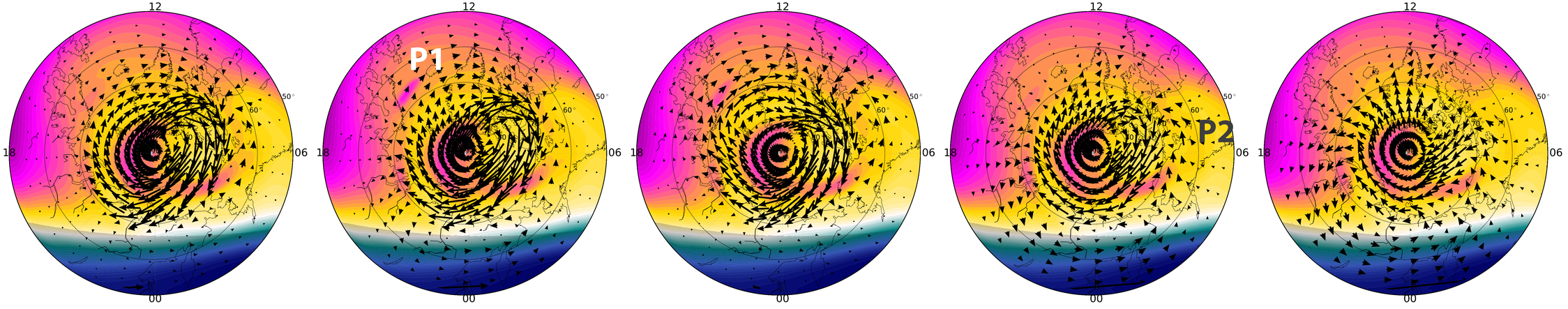

Meridional Ion Temperature

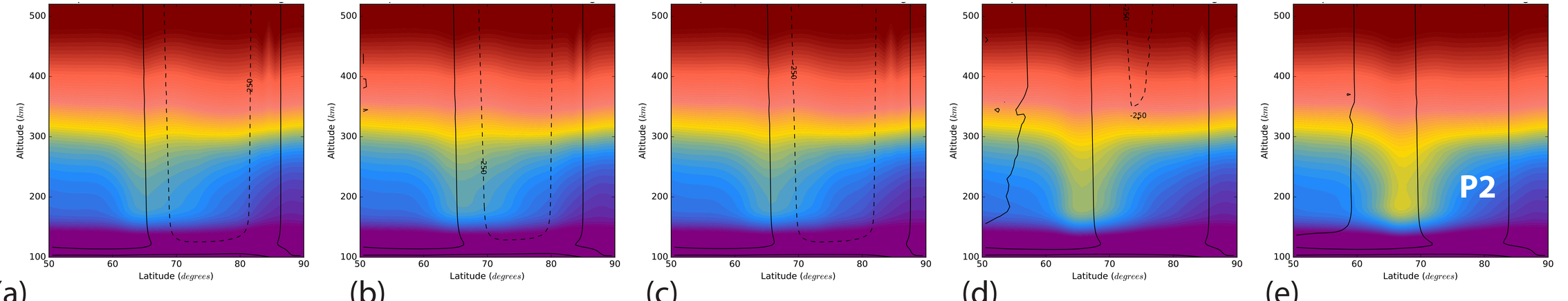

(a) (b) (c) (d) (e)

This article is protected by copyright. All rights reserved.

(a)

Variation at [Lon = 354.0 deg, Lat = 66.0] deg

P1

Altitude [km]

Ion Temperature [K]

Neutral Temperature [K]

Electron Temperature [K]

Electron Density [m^{-3}] 1e11

14:35
14:38
14:40
14:45
14:50

(b)

Variation at [Lon = 250.0 deg, Lat = 67.0] deg

P2

Altitude [km]

Ion Temperature [K]

Neutral Temperature [K]

Electron Temperature [K]

Electron Density [m^{-3}] 1e11

14:35
14:38
14:40
14:45
14:50

This article is protected by copyright. All rights reserved.

Author Manuscript

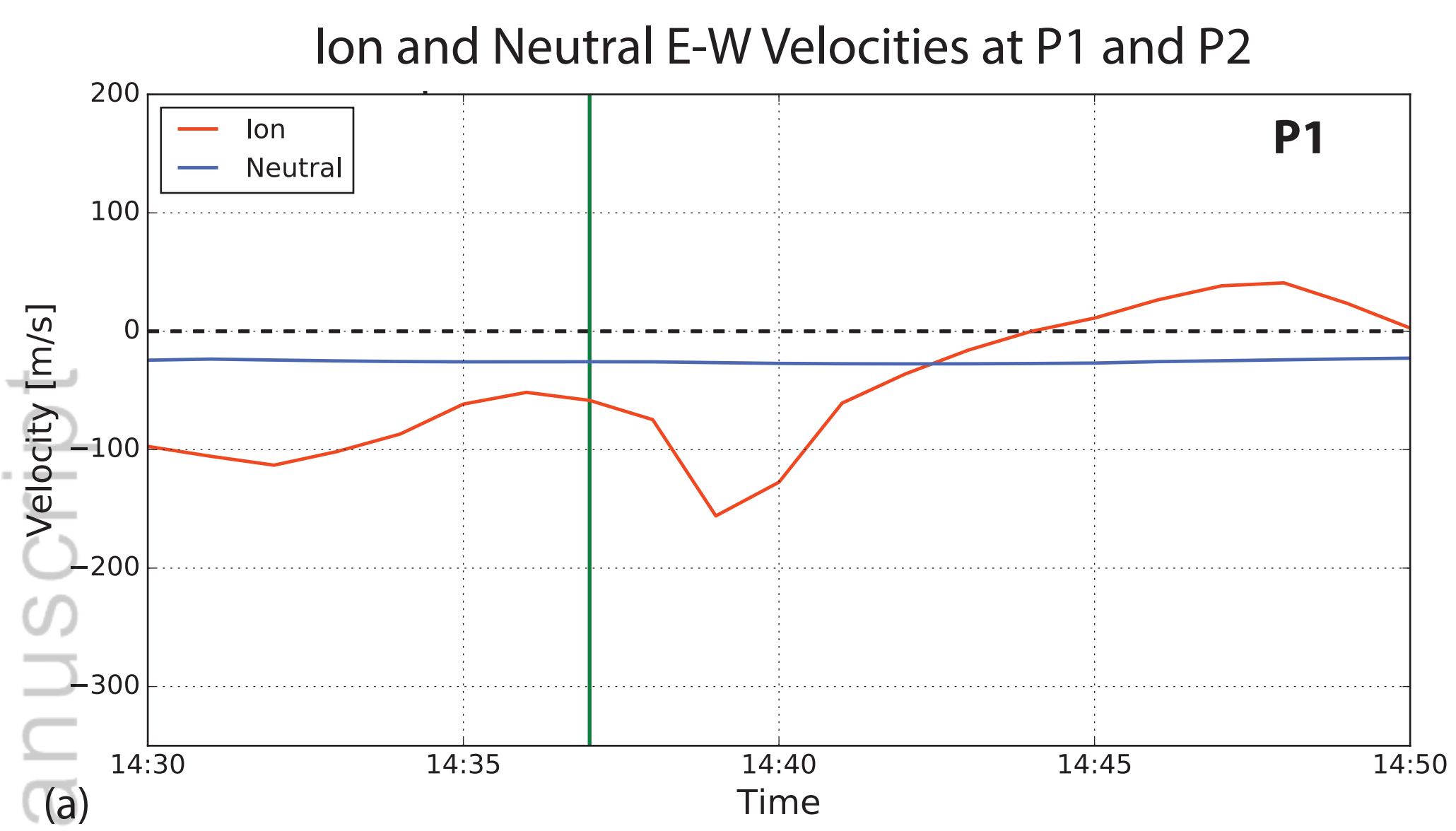

This article is protected by copyright. All rights reserved.